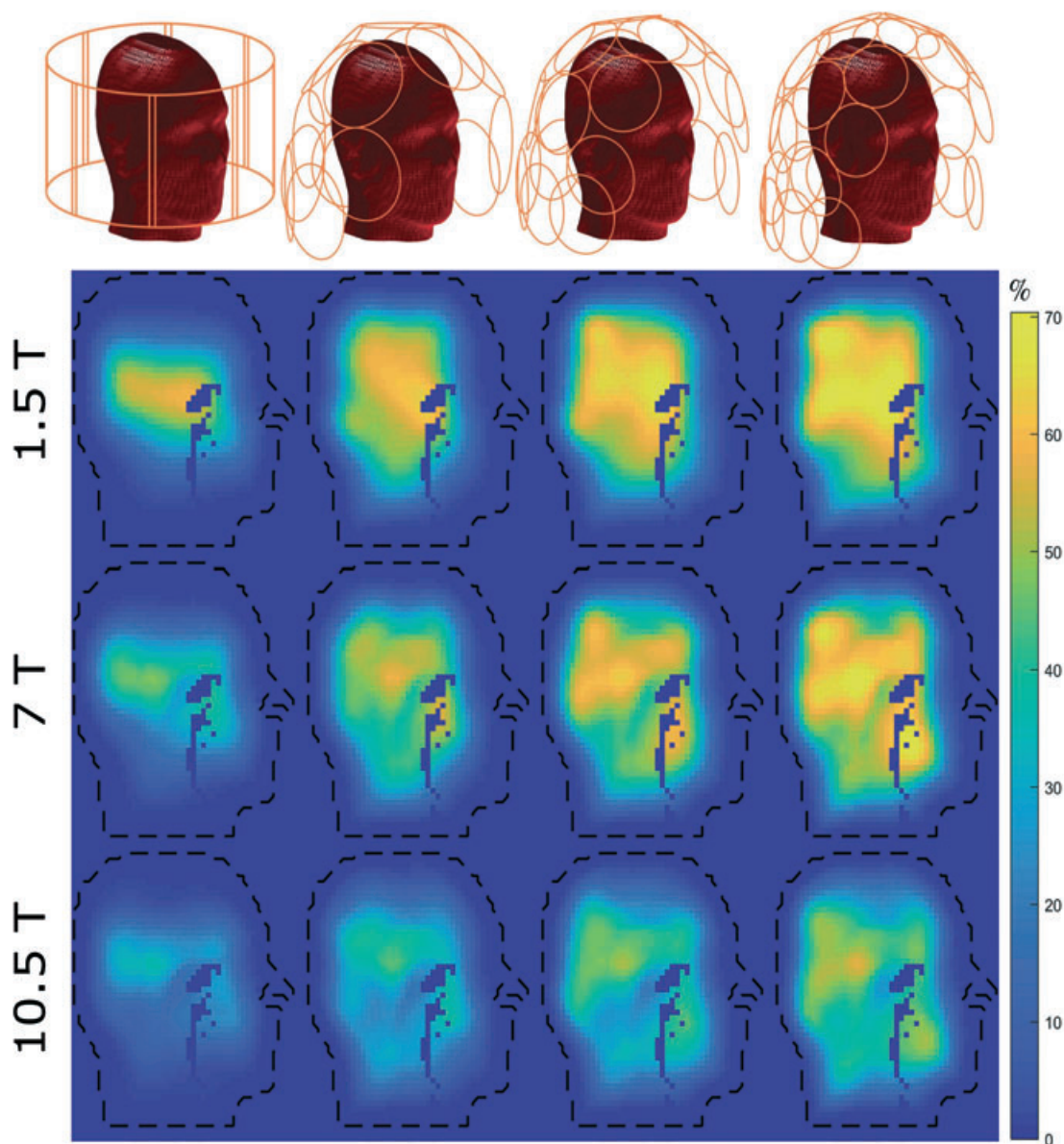


NMR IN BIOMEDICINE

Absolute Transmit Performance



RESEARCH ARTICLE

A formalism to investigate the optimal transmit efficiency in radiofrequency shimming

Ioannis P. Georgakis¹  | Athanasios G. Polimeridis²  | Riccardo Lattanzi^{3,4} 

¹Center for Computational and Data-Intensive Science and Engineering (CDISE), Skolkovo Institute of Science and Technology, Moscow, Russian Federation

²Q Bio, Redwood City, California

³Center for Advanced Imaging Innovation and Research (CAI²R) and Bernard and Irene Schwartz Center for Biomedical Imaging, Department of Radiology, New York University School of Medicine, New York, New York

⁴The Sackler Institute of Graduate Biomedical Sciences, New York University School of Medicine, New York, New York

Correspondence

Riccardo Lattanzi, Ph.D., The Bernard and Irene Schwartz Center for Biomedical Imaging, New York University Langone Health, 660 First Avenue – Room 203, New York, NY 10016, USA.
Email: riccardo.lattanzi@nyumc.org

Funding information

National Institutes of Health, Grant/Award Numbers: NIH P41 EB017183, NIH R01 EB024536, and NIH U01 EB025144; National Science Foundation, Grant/Award Number: NSF 1453675; Skoltech-MIT Next Generation Program

Transmit efficiency specifies the amplitude of the magnetic resonance excitation field produced over a region of interest with respect to the radiofrequency (RF) power deposited in the sample. This metric is highly important at ultra-high field magnetic resonance imaging (≥ 7 T), where excitation inhomogeneities and electric field interference effects could prevent achieving the desired flip angle distribution while satisfying the power safety limits. The aim of this work was to introduce an approach to calculate a theoretical upper bound on the transmit efficiency (OPTXE) for RF shimming, independent from any particular coil design. We computed the OPTXE for head-mimicking uniform spherical samples and a realistic heterogeneous head model by maximizing the square of the net transmit field per unit power deposition. The corresponding RF shimming weights were used to combine the analytical surface current modes into ideal current patterns. OPTXE grew monotonically as the target excitation voxel approached the surface of the object, and overall decreased at higher field strengths, presenting similar trends in both the uniform sphere and heterogeneous head model. Arrays with an increasing number of loops could closely approach OPTXE in the central region of the object, but performance decreased closer to the surface and at higher magnetic field strengths. The performance of 32 loops for a two-dimensional excitation region at 7 T increased from 34% to 93% when they were arranged based on the shape of the ideal current patterns. OPTXE provides an absolute reference to evaluate coil designs and RF shimming algorithms, whereas ideal current patterns could serve as guidelines for novel coil designs at ultra-high field. The uniform sphere model enables rapid analytic simulations and provides a good approximation of the OPTXE distribution in a realistic heterogeneous head model with comparable dimensions.

KEYWORDS

ideal current patterns, maximum transmit efficiency, MRI, optimal transmit efficiency, RF coil performance, RF shimming

Abbreviations used: CV, coefficient of variation; DGF, dyadic Green's function; EM, electromagnetic; ICP, ideal current patterns; MRI, magnetic resonance imaging; OPTXE, optimal transmit efficiency; RF, radiofrequency; ROI, region of interest; RWG, Rao-Wilton-Glisson; SAR, specific absorption rate; SVD, singular value decomposition; TXE, transmit efficiency; UHF, ultra-high field; UISNR, ultimate intrinsic signal-to-noise ratio.

[Correction added on 11 August 2020, after first online publication: two characters were mistakenly omitted from equation 10 and were restored.]

1 | INTRODUCTION

A common approach to assess the efficiency of a transmit coil is to evaluate the amplitude of the magnetic field (B_1^+) it produces over a region of interest (ROI) with respect to the radiofrequency (RF) power deposited in the body. Transmit efficiency (TXE) becomes highly important at ultra-high field (UHF) magnetic resonance imaging (MRI) (≥ 7 T), where B_1^+ inhomogeneities and electric field interference effects could prevent achieving the desired excitation while satisfying the safety constraints on specific absorption rate (SAR).¹ Multiple channel transmission can be used to improve the fidelity of the excitation profile and minimize SAR.^{1–4} Evaluating TXE for a transmit array requires measuring the power correlation matrix between the channels,^{5–7} in addition to the B_1^+ amplitude for each of them. Furthermore, TXE depends on the particular weighting configuration chosen to drive the distinct channels for RF shimming^{8–11} or parallel transmission.^{12–14}

Zhu et al proposed a TXE metric¹⁵ for transmit arrays, which could be used to both measure the coil performance of existing configurations and to find the optimal shimming weights that maximize TXE of a given array in a target region.¹⁶ However, while the resulting TXE would characterize the maximum performance that the particular transmit array could achieve for a given imaging task, it would not tell how much room for improvement may exist in principle, nor provide any insight into the optimal coil design that truly maximizes TXE.

It has been shown that theoretical performance limits could be used as absolute references against which to evaluate RF coil performance and to derive guidelines for optimal coil design.^{1,17–25} For example, the ultimate intrinsic signal-to-noise ratio (UISNR) could be used to assess receive arrays,^{26–29} while the associated ideal current patterns could be employed to guide coil design.^{30–33} Ultimate performance bounds were also used to investigate transmit array performance, in terms of SAR and excitation homogeneity, as a function of the number of coil elements in RF shimming and parallel transmission.^{1,34} However, they have not yet been used to obtain physical insight into optimal transmit array design.

The aim of this work is to introduce a formalism to calculate the theoretical upper bound, consistent with electrodynamic constraints, for the TXE metric described above. We named this quantity optimal transmit efficiency (OPTXE). Our goal is to provide an absolute reference to assess coil performance, independent of any particular design, and to derive new physical insights into the design of optimal transmit coils.

2 | METHODS

2.1 | The TXE metric for RF shimming

RF shimming^{10,11} was proposed to mitigate B_1^+ inhomogeneities by adequately adjusting the relative amplitudes and phases of multiple transmit elements driven with the same RF waveform. Since there are multiple possible choices for such weighting configurations, it is not straightforward to define a metric to assess the efficiency of a transmit array in RF shimming. In this work, we use the same TXE metric as Deniz et al,¹⁶ which is defined as the square of the B_1^+ magnitude within an excitation ROI per unit dissipated RF power over the entire volume of the sample^{15,16}:

$$\eta = \frac{\text{average} \|B_1^+(r)\|^2}{\frac{1}{2} \int_V \sigma(r) \|E(r)\|^2 dV}, \quad (1)$$

where $\sigma(r)$ is the conductivity of the sample. The net $B_1^+(r)$ and $E(r)$ fields at each spatial location r can be expressed as the weighted combination of the unit-current fields ($b_n^+(r)$, $e_n(r)$) of the coils of a N -channel transmit array:

$$\begin{aligned} B_1^+(r) &= \sum_{n=1}^N w_n b_n^+(r) \\ E(r) &= \sum_{n=1}^N w_n e_n(r) \end{aligned} \quad (2)$$

Here, w_n are the complex-valued RF shimming coefficients that correspond to the driving amplitude and phase modulation of the n th transmit coil. The net B_1^+ for a target excitation ROI that includes Q spatial locations, or voxels, can be written in matrix form as $\mathbf{b}_1^+ = \mathbf{C}\mathbf{w}$, where \mathbf{C} is a $Q \times N$ matrix with $C_{qn} = b_n^+(r_q)$. The average transmit field squared in the ROI can be expressed as

$$\text{average} \|B_1^+(r)\|^2 = \mathbf{w}^H \mathbf{T} \mathbf{w}, \quad (3)$$

where $\mathbf{\Gamma} = \mathbf{C}^H \mathbf{C} / Q$ is an $N \times N$ positive-definite complex Hermitian matrix, with the superscript H denoting the conjugate transpose operation. By exploiting field superposition, the total deposited, or absorbed, RF power can be calculated as

$$P_{\text{abs}} = \frac{1}{2} \int_V \sigma(\mathbf{r}) \|\mathbf{E}(\mathbf{r})\|^2 dV = \mathbf{w}^H \mathbf{\Phi} \mathbf{w}, \quad (4)$$

where $\mathbf{\Phi}$ is an $N \times N$ positive-definite complex Hermitian RF power covariance matrix whose elements are

$$\Phi_{ij} = \frac{1}{2} \int_V \sigma(\mathbf{r}) \mathbf{e}_i^*(\mathbf{r}) \cdot \mathbf{e}_j(\mathbf{r}) dV \quad (5)$$

with $i, j \in \{1, \dots, N\}$ and the superscript * denoting the complex conjugation. By substituting Equations 3 and 4, the TXE metric in Equation 1 can be rewritten as the ratio of two quadratic forms

$$\eta = \frac{\mathbf{w}^H \mathbf{\Gamma} \mathbf{w}}{\mathbf{w}^H \mathbf{\Phi} \mathbf{w}} \quad (6)$$

with units of $(\mu\text{T})^2/W$. The problem of finding the maximum of η can be treated as a generalized eigenvalue problem ($\mathbf{\Gamma} \mathbf{w} = \lambda \mathbf{\Phi} \mathbf{w}$), which has a closed-form solution and guarantees finding a global optimum.^{15,16,35} More specifically, the largest eigenvalue corresponds to the maximum TXE (η_{max}) and the associated eigenvector gives the corresponding RF shimming weights (\mathbf{w}_{max}) that yield the maximum TXE. Note that in the case of a single transmit channel, the matrices $\mathbf{\Gamma}$ and $\mathbf{\Phi}$ reduce to scalars, and the metric captures B_1^+ strength squared per unit power, which is compatible with the conventional approach to evaluate TXE as the amplitude of B_1^+ divided by the square root of absorbed power.

2.2 | An upper bound on TXE

In order to calculate the theoretically largest value for the chosen TXE metric (ie, the OPTXE), independent of any particular coil design, we employed a basis of orthogonal electromagnetic (EM) current modes flowing on a surface surrounding the sample as the elements of a hypothetical infinite array.^{1,18–22,25,31} The equations introduced above for the case of finite arrays remain valid, with N indicating the number of modes instead of coils. According to the surface equivalence, or Huygens's, principle, any EM field distribution inside the source-free volume contained by a closed surface can be generated by a current distribution flowing on the surface.³⁶ Since the operator that maps surface electric currents to incident EM fields over the object is compact,³⁷ TXE is guaranteed to converge to its largest value, which is the OPTXE, as the number of basis current modes is increased. This property, which can be exploited both for the case of analytical computations in uniform spherical samples and numerical computations in heterogeneous head models,³⁸ allowed us to use a finite number of modes to compute the OPTXE.

2.3 | OPTXE in a head-mimicking uniform sphere

We used a simulation framework³¹ based on dyadic Green's functions (DGFs),³⁹ which enables the rapid analytic calculation of the OPTXE in a homogeneous spherical sample. The method begins by defining a current distribution on a spherical surface with radius b , surrounding a uniform sphere^{31,39}:

$$\mathbf{J}(r, \theta, \varphi) = \kappa(\theta, \varphi) \frac{\delta(r-b)}{b^2 \sin \theta}, \quad (7)$$

where r (radial), θ (polar) and φ (azimuthal) are spherical coordinates and κ is the surface current density, which can be expressed as a weighted sum of basis current modes^{31,40}:

$$\kappa(\theta, \varphi) = \sum_{l=0}^{l_{\text{max}}} \sum_{m=-l}^l -i \sqrt{l(l+1)} \left[W_{l,m}^{(M)} \mathbf{X}_{l,m}(\theta, \varphi) + W_{l,m}^{(E)} \hat{\mathbf{r}} \times \mathbf{X}_{l,m}(\theta, \varphi) \right]. \quad (8)$$

Here, l and m are mode indices, l_{\max} is the expansion order, $i = \sqrt{-1}$ is the imaginary unit, \hat{r} is the unit vector in the radial direction and $X_{l,m}$ is a vector spherical harmonic (Appendix A.1). $W_{l,m}^{(M)}$ and $W_{l,m}^{(E)}$ are the complex-valued series expansion coefficients for the magnetic-type (divergence-free) and electric-type (curl-free) surface current contributions, respectively. The net EM field generated by the current modes inside the sphere can be calculated using the appropriate DGF (Appendix A.1) as

$$\begin{aligned} \mathbf{E}(\mathbf{r}) &= -\omega\mu_0k_0 \sum_{l=0}^{+\infty} \sum_{m=-l}^l [\mathbf{M}_{l,m}(k_{in}, \mathbf{r}) V_{l,m}^M + \mathbf{N}_{l,m}(k_{in}, \mathbf{r}) V_{l,m}^N] \\ \mathbf{B}(\mathbf{r}) &= -i\mu_0k_0k_{in} \sum_{l=0}^{+\infty} \sum_{m=-l}^l [\mathbf{N}_{l,m}(k_{in}, \mathbf{r}) V_{l,m}^M + \mathbf{M}_{l,m}(k_{in}, \mathbf{r}) V_{l,m}^N]. \end{aligned} \quad (9)$$

Here, ω is the angular frequency, μ_0 is the free-space permeability, $k_0 = \omega\sqrt{\mu_0\epsilon_0}$ is the free-space wavenumber and ϵ_0 is the free-space permittivity. Also, $k_{in} = k_0\sqrt{\epsilon_r - \frac{i\sigma}{\omega\epsilon_0}}$ is the complex wavenumber inside the lossy, dielectric sphere with relative permittivity ϵ_r and electric conductivity σ . $\mathbf{M}_{l,m}$ and $\mathbf{N}_{l,m}$ are spherical vector wave functions used to construct the DGF, whereas $V_{l,m}^M$ and $V_{l,m}^N$ are weighting coefficients derived by multiplying the series expansion coefficients by a transformation matrix \mathbf{T} , which accounts for boundary conditions at the surface of both the spherical sample and the current-bearing spherical surface. By treating the current modes as elements of a transmit array, we could use the fields in Equation 9 to construct the matrices $\mathbf{\Gamma}$ and $\mathbf{\Phi}$ in Equations 3 and 4, respectively (Appendix A.2). The number of modes was then increased until the largest eigenvalue, which can be computed numerically (eg, with the Matlab function `eigs` [$\mathbf{\Gamma}$, $\mathbf{\Phi}$, 1]), converged to its maximum value $\tilde{\eta}$. The corresponding eigenvector ($\tilde{\mathbf{w}}$), which contains the RF shimming coefficients ($W_{l,m}^{(M)}$ and $W_{l,m}^{(E)}$), was substituted in Equation 8 to calculate the ideal current patterns (ICP) yielding OPTXE as a weighted combination of the surface current modes.^{23,31}

OPTXE calculations were performed for spherical samples with uniform, frequency-dependent electrical properties, mimicking average brain gray and white matter³⁸ for various magnetic field strengths (Table 1). We simulated spherical objects with different radii $a = 7.5, 10$ and 15 cm. The radius of the current-bearing spherical surface was set as $b = a + D$, with $D = 1.5$ cm in all cases (Figure 1A). We calculated OPTXE and ICP for single voxel locations across the diameter of the sample, as well as for two-dimensional (2D) circular excitation ROIs, centered in the axial plane, and three-dimensional (3D) spherical excitation ROIs, concentric with the sample (Figure 1B). For both types of ROI, we considered different radii: $0.3a$, $0.6a$ and $0.9a$. Using the same formalism, we also searched for the eigenvector that minimizes B_1^+ inhomogeneity and compared the resulting TXE, B_1^+ uniformity and ICP with those for the optimal case. We used an expansion order $l_{\max} = 45$, which ensured convergence of all calculations (Figures S3, S4 and S5).

2.4 | OPTXE in a realistic heterogeneous head model

We cropped the head of the Duke numerical body model³⁸ and discretized it using 5 mm voxel resolution (Figure 1C). We employed electric surface currents distributed on a perfectly electrically conducting spherical shell enclosing the head model. We discretized the current distribution using a triangulated grid with Rao-Wilton-Glisson (RWG)⁴¹ basis functions $\mathbf{f}_n(\mathbf{r})$. For every n RWG basis element of the triangulated shell we computed the incident electric field and magnetic flux density at all q voxels of the head model, using the free-space DGF to form the shell-to-head coupling matrices \mathbf{N} and \mathbf{K} :

$$\begin{aligned} \mathbf{N}_{qn} &= \mathbf{E}_n^{\text{inc}}(\mathbf{r}_q) = i\omega\mu_0 \int_{S'} \bar{\mathbf{G}}_{EJ}(\mathbf{r}_q, \mathbf{r}') \cdot \mathbf{f}_n(\mathbf{r}') dS' \\ \mathbf{K}_{qn} &= \mathbf{B}_n^{\text{inc}}(\mathbf{r}_q) = -\mu_0 \int_{S'} \bar{\mathbf{G}}_{HJ}(\mathbf{r}_q, \mathbf{r}') \cdot \mathbf{f}_n(\mathbf{r}') dS', \end{aligned} \quad (10)$$

TABLE 1 Dielectric properties of average brain tissue

Bo [T]	0.5	1.5	3	7	10.5	14	21
Larmor frequency [MHz]	21.3	63.9	127.7	298.0	447.0	596.1	894.1
Dielectric constant ϵ_r	157.5	82.7	63.1	51.9	49.1	47.6	45.9
Conductivity σ [1/Ωm]	0.30	0.40	0.46	0.55	0.61	0.66	0.76

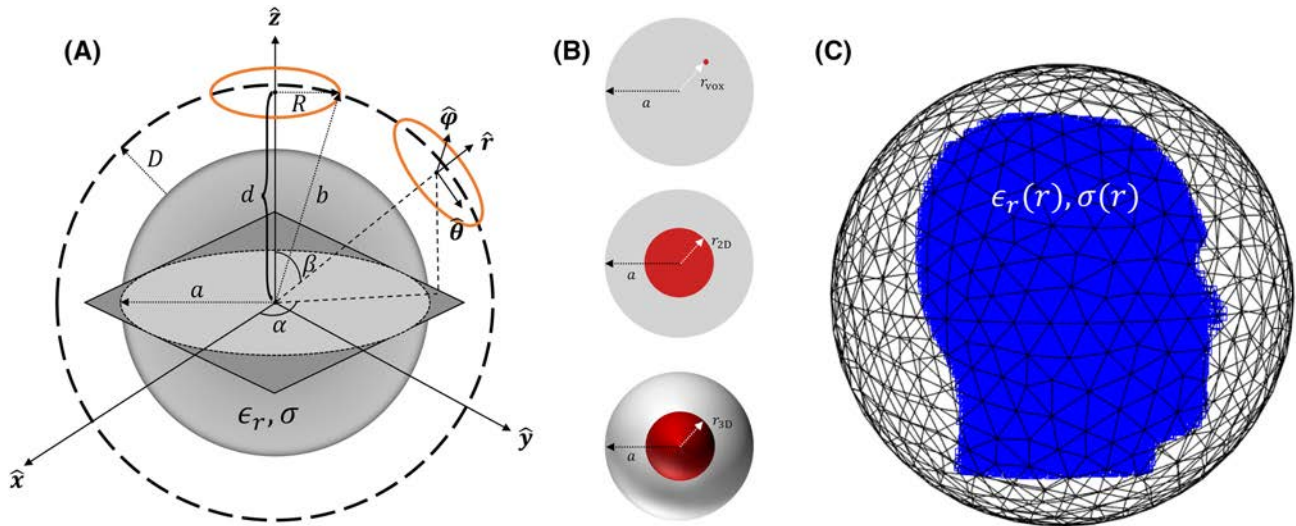


FIGURE 1 Sample geometries and relevant simulation settings. A, schematic representation of the homogeneous spherical sample with frequency-dependent electrical properties ϵ_r, σ and radius a surrounded by a current-bearing 2D spherical surface with radius b . Circular loop coils (orange) with radius R are arranged on the spherical surface and can be appropriately rotated by azimuthal (α) and polar (β) angles to compose different finite arrays designs. B, optimal transmit efficiency (OPTXE) was calculated for single voxels across the diameter of the sample, 2D circular disk excitation ROIs on a transverse plane through the center of the object, and 3D spherical excitation ROIs concentric with the spherical sample. C, schematic representation of the “Duke” inhomogeneous realistic head model surrounded by a triangulated current-bearing spherical shell

where the DGFs that map electric current sources to observed electric fields and magnetic fields were calculated, respectively, as:

$$\begin{aligned}\bar{\mathbf{G}}_{EJ}(\mathbf{r}, \mathbf{r}') &= \left(\bar{\mathbf{I}} + \frac{\nabla \nabla}{k_0^2} \right) g(\mathbf{r}, \mathbf{r}') \\ \bar{\mathbf{G}}_{HJ}(\mathbf{r}, \mathbf{r}') &= \nabla g(\mathbf{r}, \mathbf{r}') \times \bar{\mathbf{I}},\end{aligned}\quad (11)$$

with $g(\mathbf{r}, \mathbf{r}') = \frac{e^{ik_0|\mathbf{r}-\mathbf{r}'|}}{4\pi|\mathbf{r}-\mathbf{r}'|}$ denoting the free-space scalar wave Green's function and $\bar{\mathbf{I}}$ the identity dyadic. The coupling matrices in Equation 10 are low rank due to the smoothing property of the Green's functions for remote elements interactions,³⁷ which allowed us to use a truncated singular value decomposition (SVD) to approximate them with a prescribed approximation error. In particular, we applied SVD to the coupling matrix, $\mathbf{K} = \mathbf{U}\mathbf{S}\mathbf{V}^*$, and truncated with 10^{-5} relative tolerance. This step can be considered equivalent to generating an orthonormal numerical basis of incident magnetic flux densities. All possible incident magnetic flux densities can then be expressed as a linear combination of these basis modes with an accuracy up to the aforementioned specified tolerance, using $\mathbf{b}^{\text{inc}} = \mathbf{U}\mathbf{a}$, where \mathbf{a} denotes the weighting coefficients. The corresponding orthogonal incident electric fields basis is derived as $\mathbf{e}^{\text{inc}} = \mathbf{N}\mathbf{V}\mathbf{S}^{-1}\mathbf{a}$. Finally, we used an in-house volume integral equation solver with piecewise linear basis functions⁴² to compute the total (incident plus scattered) EM fields in the realistic heterogeneous head model for each incident electric field basis vector. While $\bar{\mathbf{\Gamma}}$ (Equation 3) can be calculated directly from the total magnetic field, Φ was computed with a numerical integration quadrature scheme that included the contributions of the piecewise linear terms. As for the analytic case, the number of modes was increased until the largest eigenvalue converged to the OPTXE. OPTXE maps were calculated for different field strengths, adjusting the electrical properties of the numerical head model to the corresponding Larmor frequency.

2.5 | Maximum TXE for finite arrays

For the case of a uniform dielectric sphere, the maximum TXE of finite coil arrays can be calculated within the same analytic DGF framework used for the OPTXE, by appropriate weighted combinations of the basis modes in Equation 8. In particular, the weights to simulate circular loop coils can be derived analytically³¹:

$$W_{l,m}^{\text{loop},(M)} = -\frac{2\pi R}{l+1} \sqrt{\frac{4\pi}{2l+1}} Y_{l,m}^*(\beta, \alpha) \left(\cot\theta Y_{l,0}(\theta, \varphi) - \sqrt{\frac{2l+1}{2l-1}} \csc\theta Y_{l-1,0}(\theta, \varphi) \right) \Big|_{\theta = \arccos \frac{d}{\sqrt{d^2 + R^2}}} \quad (12)$$

$$W_{l,m}^{\text{loop},(E)} = 0,$$

where α and β define the angular position of the center of the loop coil on the current-bearing spherical surface, d is the distance from the center of the spherical sample to the center of the loop coil and R is the radius of the loop coil (Figure 1A). The B_1^+ and RF power covariance matrices for the loop array can be calculated in a straightforward manner by applying the weights in Equation 12 to the corresponding matrices for the full set of modes.

For the case of the realistic head model, the incident EM fields of finite coil arrays can be modeled within a simplified wire integral equation framework, where each segment of a coil is assumed to have a constant current, proportional to its length, radiating in free space. Then the total EM fields can be computed with the same volume integral equation solver⁴² as for the basis fields. The maximum TXE for the array is then computed as for the basis functions by solving the generalized eigenvalue problem.

We investigated the TXE of various loop arrays, as a percentage of the OPTXE, for different values of the main magnetic field strength. For the case of the uniform sphere, we calculated the maximum TXE for different excitation ROIs for arrays with an increasing number (8, 16, 24, 32) of fully encircling loops, as well as belt-shaped arrays with an increasing number (8, 16, 24, 32) of loops symmetrically arranged around the central axial plane of the spherical sample. For the case of the head model, we designed an array with eight loops arranged on a cylindrical surface surrounding the sample and three helmet-shaped arrays with 16, 24 and 32 loops.

3 | RESULTS

The OPTXE for single voxels along the sphere diameter exponentially increased as the target voxel approached the surface of the sphere (Figure 2), displaying a similar trend to that reported for the UISNR.^{20,21} The OPTXE decreased as the main magnetic field increased, but, for target voxels in the central region of the sphere, began to gradually increase again for field strengths greater than 7 T, especially for small samples. For example, OPTXE at the center was 4.9 and 2.57 ($\mu\text{T}^2/\text{W}$) at 7 T for the spheres with $a = 7.5$ and 10 cm, respectively, while it was 9.55 and 3.39 ($\mu\text{T}^2/\text{W}$) at 21 T, corresponding to 95% and 32% improvements, respectively. Figure 3 shows a temporal snapshot ($\omega t = 0$) of the density of ICP yielding OPTXE at various voxel locations for different field strengths. Video S1 shows how the same ICP evolve over time. Note that, similar to the case of UISNR,³¹ the ICP for OPTXE at the central voxel took the form of two large distributed loops precessing at Larmor frequency at every field strength, whereas they alternated between distributed single-loop and figure-of-eight shapes for intermediate voxels, becoming increasingly complex at higher field strengths.

The OPTXE for increasing size of the 2D excitation ROI is shown in Figure 4. Except for small ROIs, where behavior aligns with that reported for the central voxel (Figure 2), OPTXE decreased with increasing field strength for all sphere radii. Interestingly, at low field (0.5, 1.5 and 3 T) the OPTXE was constant until the size of the ROI was $\sim 0.65a$. For larger ROI sizes, OPTXE increased double-exponentially, although leading to

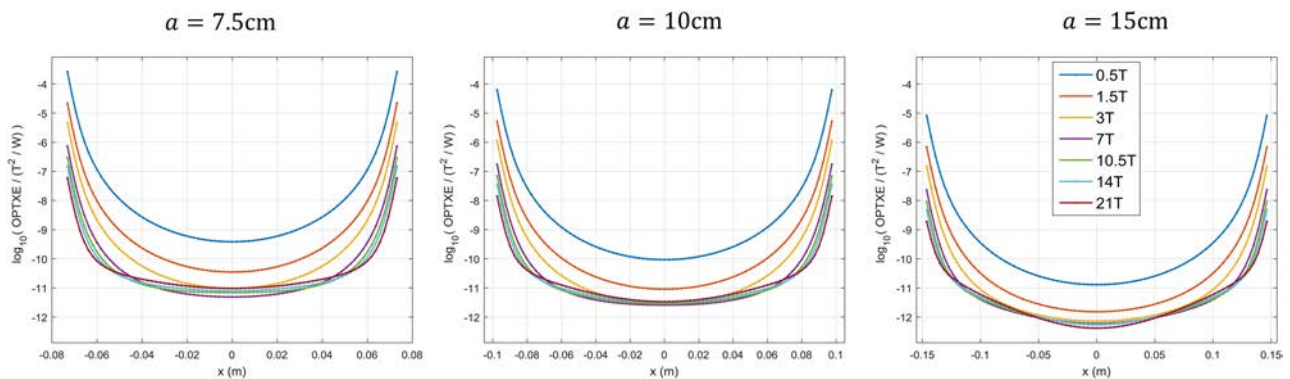


FIGURE 2 Optimal transmit efficiency (OPTXE) as a function of voxel position for different spherical sample size and magnetic field strength. OPTXE is plotted in logarithmic scale across the diameter of spherical samples with radii $a = 7.5, 10$ and 15 cm and brain-mimicking electrical properties at the corresponding magnetic field strengths $B_0 = 0.5, 1.5, 3, 7, 10.5, 14$ and 21 T. OPTXE decreases for larger objects and as the magnetic field strength increases up to 7 T. At voxels closer to the center, OPTXE increases again for magnetic field strengths > 7 T, except for the largest sphere. Near the edge of the spherical sample, OPTXE is order of magnitudes higher than at the center, for all object sizes and field strengths

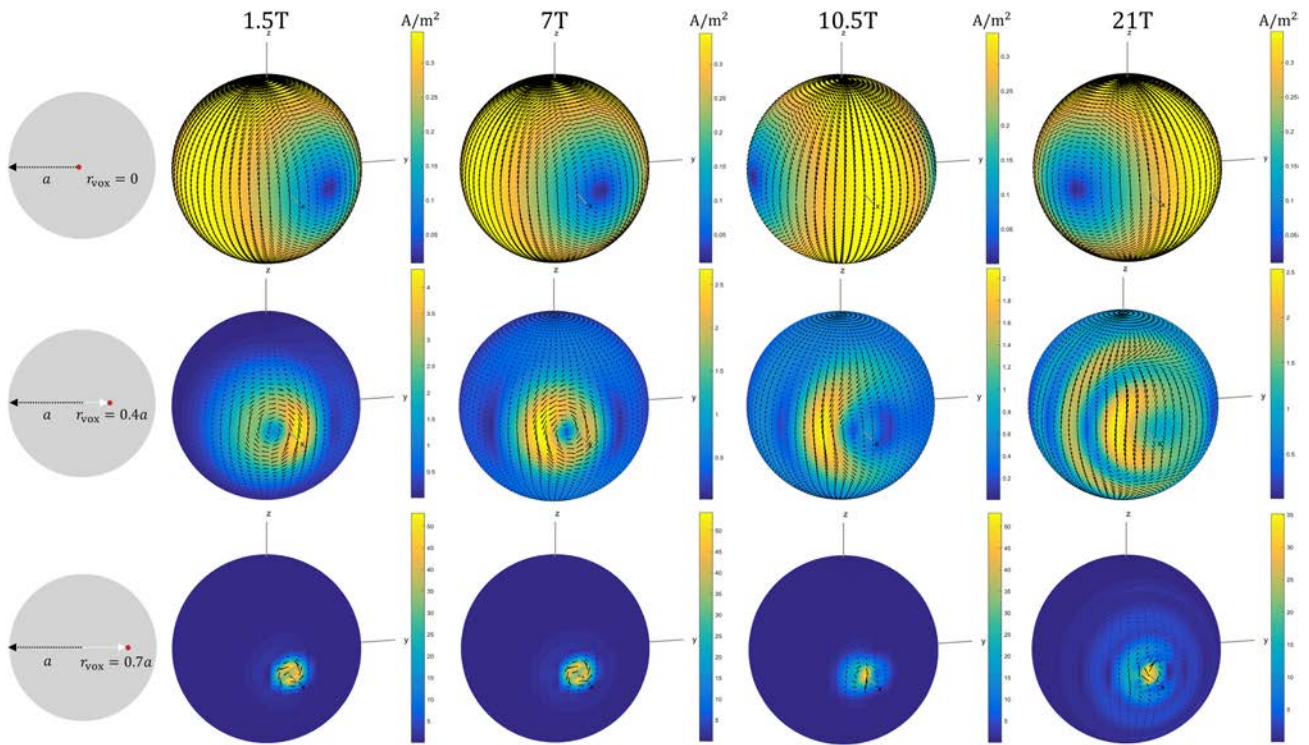


FIGURE 3 Snapshots of ideal current patterns yielding the optimal transmit efficiency (OPTXE) at different voxel positions for various main magnetic field strengths. The density of ideal current patterns at $\omega t = 0$ is shown for the spherical sample with radius $a = 10$ cm, for voxels at the center ($r_{\text{vox}} = 0$), at an intermediate position ($r_{\text{vox}} = 0.4a$), and near the surface ($r_{\text{vox}} = 0.7a$). The voxel positions are shown in the first column. The other columns show the corresponding ideal current patterns for increasing $B_0 = 1.5, 7, 10.5$ and 21 T. The shape and density of the ideal current patterns vary significantly among different voxel positions. Specifically, at the center, they resemble two large distributed loops on opposite sides of the sphere precessing at the Larmor frequency for all field strengths. At the intermediate and near-the-surface positions, they become increasingly localized around the target voxel. As the magnetic field increases, their shape becomes more complex, especially for intermediate voxel positions

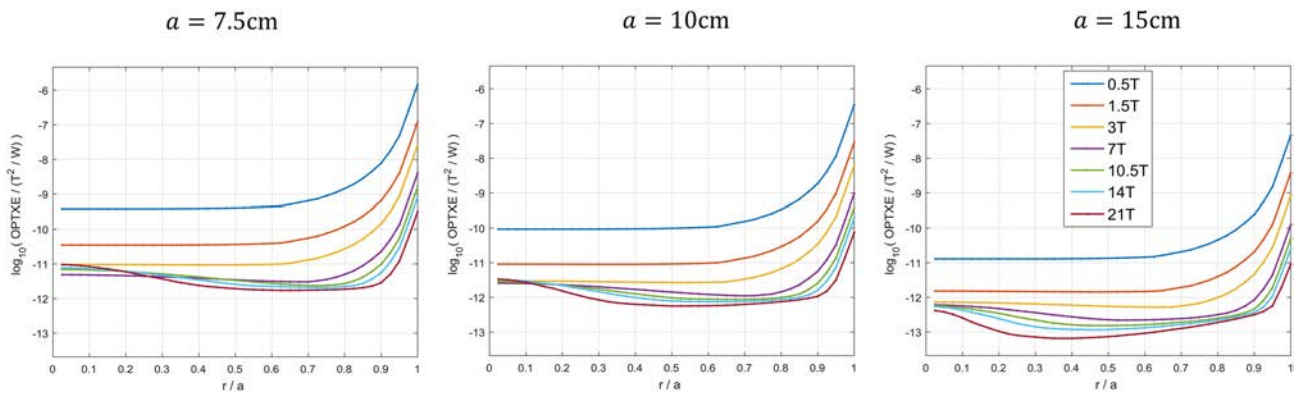


FIGURE 4 Optimal transmit efficiency (OPTXE) as a function of the size of the two-dimensional (2D) excitation region of interest (ROI) for different spherical sample size and magnetic field strength. OPTXE is plotted in logarithmic scale for spherical samples with radii $a = 7.5, 10$ and 15 cm and brain-mimicking electrical properties, adjusted for each magnetic field strength. The OPTXE is higher for smaller object sizes. The OPTXE in 2D ROIs remains approximately constant until the ROI size approaches the diameter of the sphere section, at which point it starts to rapidly increase due to the contributions of the edge voxels where OPTXE is high (see Figure 2)

impractical results, as shown in Figure 5 and described in the Discussion. At field strengths equal to or greater than 7 T, the OPTXE had a global minimum that corresponded to smaller ROI sizes as B_0 increased. In particular, for the case of a spherical sample with $a = 10$ cm, global minima were found for $r_{2D} = 0.7a, 0.675a, 0.625a$ and $0.5a$ at $7, 10.5, 14$ and 21 T, respectively. For the larger object ($a = 15$ cm), global minima at the same field strengths corresponded to $r_{2D} = 0.525a, 0.45a, 0.4a$ and $0.375a$.

Figure 5 compares MR excitations for the largest eigenvector that maximizes TXE vs. the eigenvector that minimizes B_1^+ inhomogeneity. In the case of an ROI radius of $0.8a$, using the fifth eigenvector resulted in a coefficient of variation (CV) of 24% for B_1^+ within the ROI, compared with 58% when using the largest (first) eigenvector, while still achieving 84% of the OPTXE. The tradeoff associated with improving B_1^+ homogeneity is higher for an ROI radius of $0.9a$, where decreasing the CV of B_1^+ from 152% to 94% corresponds to giving up $\sim 50\%$ of the OPTXE. When the radius of the ROI is equal to the radius of the sphere, it is not possible to reduce B_1^+ variability without losing nearly all TXE. Note that in the case of ROIs with a radius up to $0.7a$, the largest eigenvalue maximizes TXE while achieving excellent B_1^+ homogeneity within the ROI.

Figure 6 shows temporal snapshots of ICP yielding OPTXE in a small and a large 2D ROI for various field strengths. Video S2 shows the corresponding full-time evolution. For the small ROIs, the ICP resembled large distributed loops precessing at the Larmor frequency, whereas for

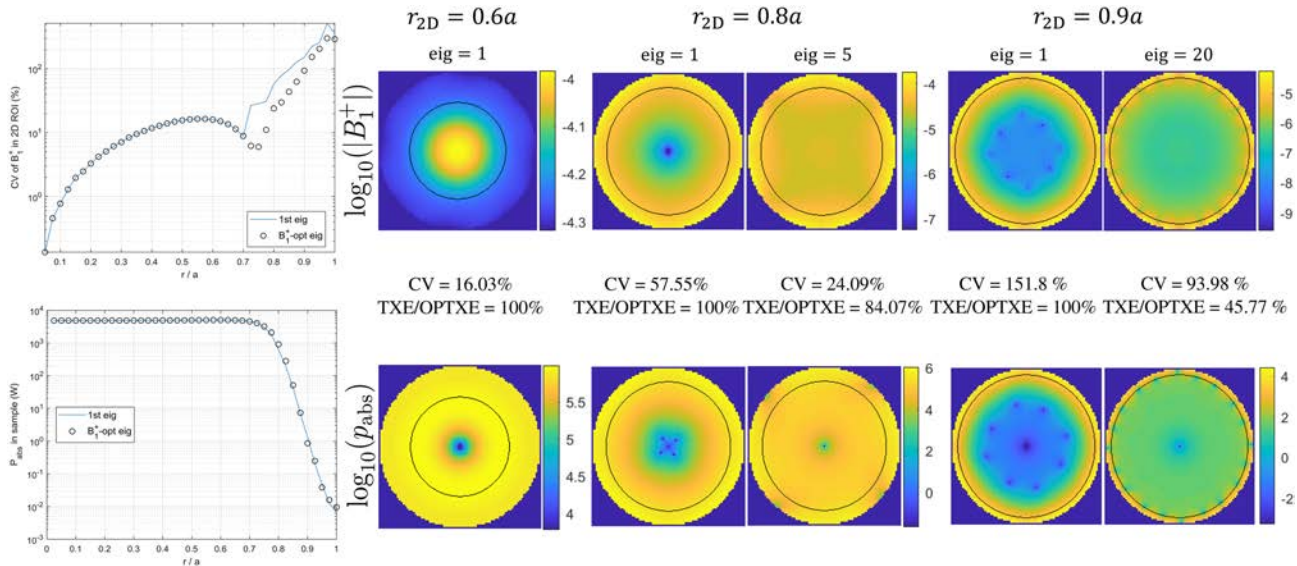


FIGURE 5 Comparison of B_1^+ and absorbed RF power distributions associated with the first eigenvector (i.e., optimal transmit efficiency [OPTXE]) and the eigenvector that minimizes B_1^+ inhomogeneity within a 2D excitation ROI. The largest eigenvalue that maximizes TXE also minimizes the coefficient of variation (CV) of B_1^+ within the ROI until $r_{2D} = 0.7a$. For larger ROIs, the eigenvector that maximizes B_1^+ homogeneity results in slightly lower TXE and increased RF power deposition. When the radius of the ROI approaches the radius of the spherical sample it is more difficult to achieve a homogeneous B_1^+ distribution

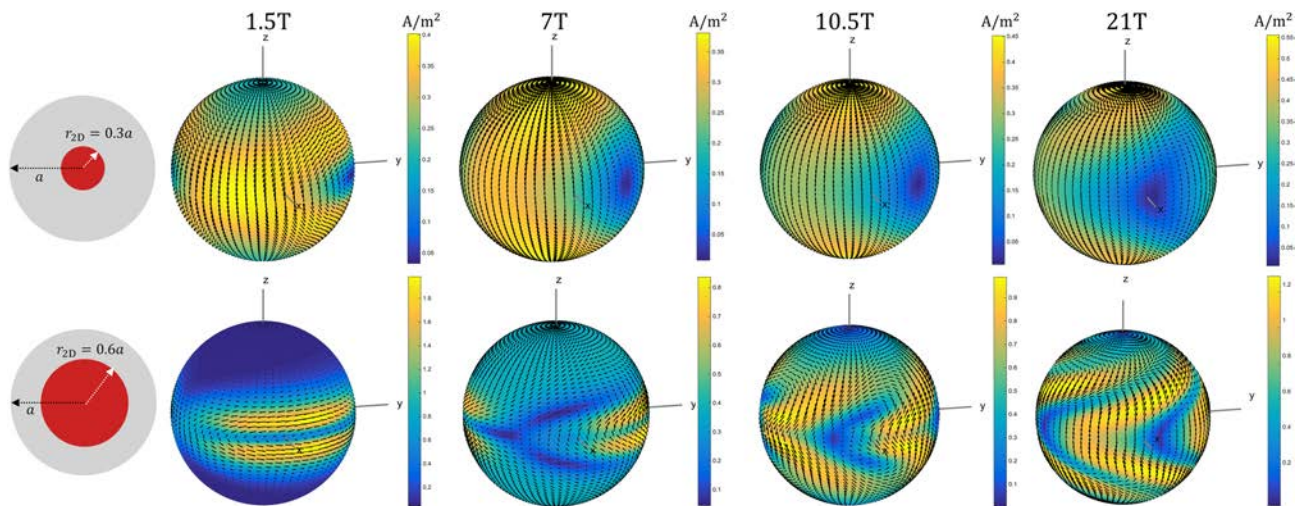


FIGURE 6 Snapshots of ideal current patterns yielding the optimal transmit efficiency (OPTXE) for two sizes of the two-dimensional (2D) excitation ROI and different main magnetic field strengths. The density of ideal current patterns at $\omega t = 0$ is shown for the spherical sample with radius $a = 10$ cm, and for circular disk ROIs of size $r_{2D} = 0.3a$ and $r_{2D} = 0.6a$. The corresponding 2D ROIs are shown in the schematics of the first column. The shape and density of the ideal current patterns differ significantly as the 2D ROI size changes. Specifically, at $r_{2D} = 0.3a$, they resemble two compressed distributed loops of elliptical shape on opposite sides of the sphere precessing at the Larmor frequency. For the larger 2D ROI, the eccentricity of the elliptical shape also increases, and the ideal current patterns become more localized around the excitation plane. As the magnetic field strength increases, the ideal current patterns become more complex, with wave and propagation delay affecting their shape

the large ROIs the patterns became more localized around the excitation plane, taking the shape of ellipses. As the operating frequency increased, propagation delay and wave phenomena affected the shape of the ICP. The behavior of OPTXE for 3D excitation ROIs of increasing size resembled that observed for 2D ROIs (Figures S1, S2 and S5).

Figure 7 shows the absolute transmit performance ($100 \cdot \text{TXE}/\text{OPTXE}$) of encircling arrays of loops at every voxel in the central axial plane, for different magnetic field strengths. In all cases, OPTXE was approached more closely as the number of loops increased. However, overall array performance decreased at higher fields, suggesting that more coils and different type of coils, for example, electric dipoles,⁴³ may be needed to approach the OPTXE. While at 3 T, eight and 32 loops achieved 95% and 99%, respectively, of the OPTXE at the central voxel, the performance of the same arrays was 50% and 96% at 10.5 T. The performance at high field dropped considerably for intermediate voxel locations. For example, at $r_{\text{vox}} = 0.5a$, eight and 32 loops yielded 31% and 80% performance, respectively, at 3 T, but reached only 16% and 56% of the optimum at 10.5 T. Figure 8 explores the performance of belt-shaped arrays with different numbers of elements for maximum TXE inside 2D ROIs of increasing size. As for the individual voxel optimizations (Figure 7), we found an inverse relationship between field strength and performance, and a direct one between the number of elements and performance. In particular, at 3 T all arrays could achieve close to 100% performance for certain sizes of the excitation ROI, whereas at 10.5 T at least 24 loops were needed to achieve more than 80% performance. While OPTXE was approximately constant for increasing sizes of the 2D ROIs (Figure 4), the performance of the belt-like arrays varied significantly. At all field strengths, array performance was maximal for an ROI with a radius greater than 50% of the sphere radius, with such optimal ROI size increasing with main magnetic field strength.

Figure 9 compares the spatial distribution of the OPTXE in the heterogeneous head model and the uniform sphere at different field strengths. The uniform sphere had a radius of 10 cm to match the dimension of the head model along the y-axis. At the center of the head, OPTXE decreased from 19.5 to 2.95 and 2.69 (μT^2)/W when the field strength increased from 1.5 to 7 and 10.5 T, respectively, corresponding to decreases of 85% and 86%. The corresponding OPTXE values at the center of the sphere at 1.5, 7 and 10.5 T were 9.12, 2.57 and 2.82 (μT^2)/W,

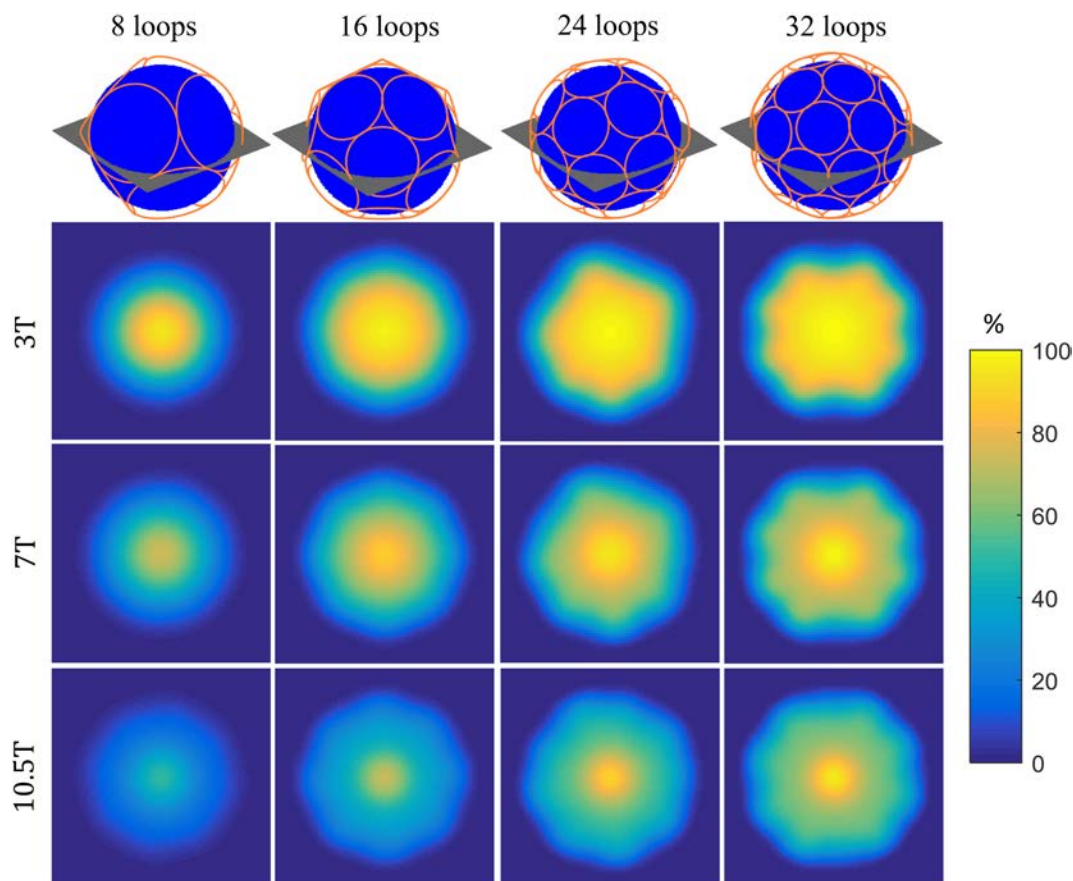


FIGURE 7 Absolute transmit performance of finite arrays with an increasing number of elements encircling the spherical sample at different main magnetic field strengths. Performance maps displaying maximum TXE as a percentage of the OPTXE at each voxel of the central axial plane of the spherical sample with $a = 10\text{cm}$ are shown for various finite arrays and for increasing B_0 . Absolute transmit performance is higher over a broader region when the number of transmit loops increases, but more than 32 elements seem to be required to approach the optimal performance at higher magnetic field strengths

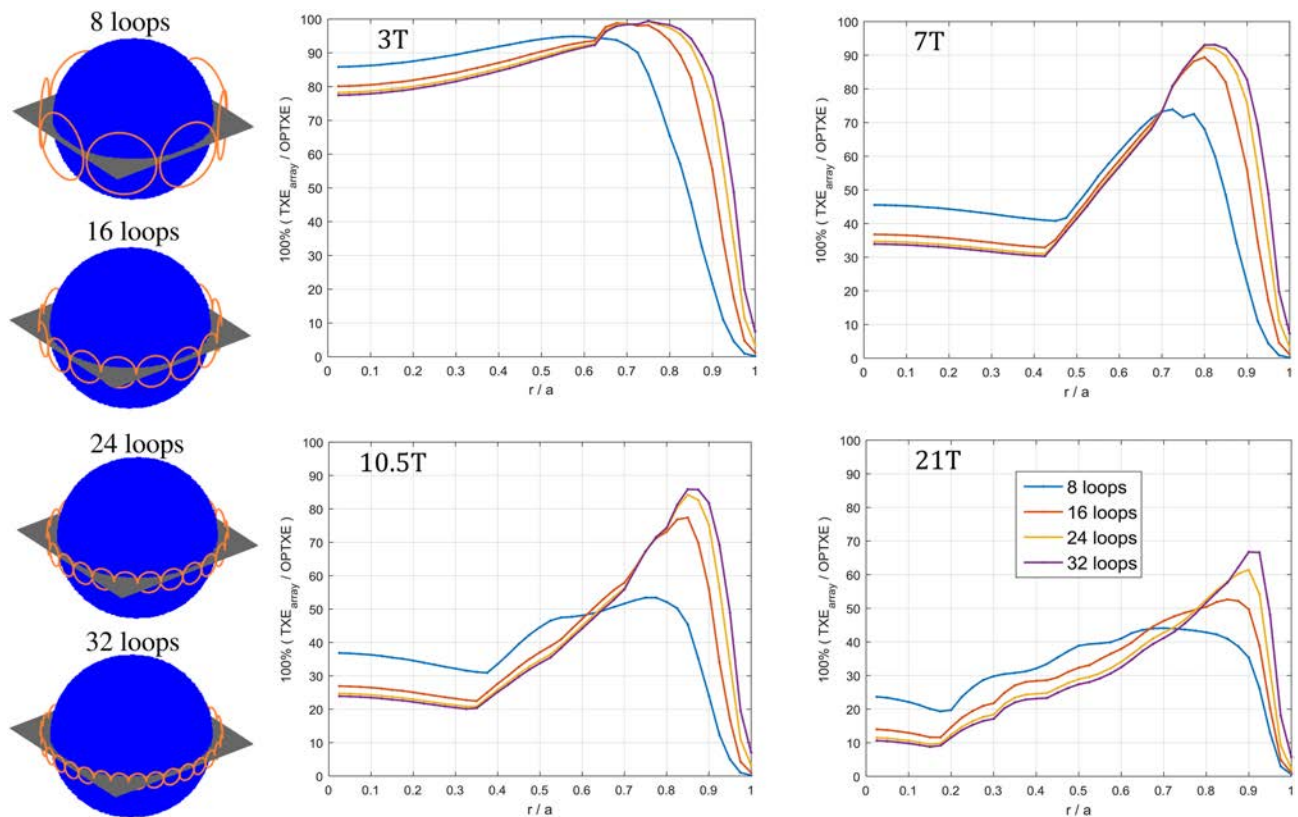


FIGURE 8 Absolute transmit performance of finite arrays with an increasing number of elements arranged like a belt around the central plane of the spherical sample, as a function of the size of the 2D excitation ROI. Schematics of the finite arrays are shown in the first column. Array performance is plotted as a percentage of the OPTXE for increasing size of the 2D circular disk excitation ROI for the spherical sample with $a = 10$ cm. Absolute transmit performance is higher when the array configuration is more consistent with the shape of the ideal current patterns (Figure 6). Array performance increases with the number of elements, but decreases at higher field strength

respectively. The central OPTXE profile for the head-mimicking sphere and the realistic head model almost overlapped along the dimension of the head that matched the diameter of the sphere (ie, the y-profile).

The performance maps for finite arrays with increasing number of transmit coils were also similar between the uniform sphere (Figure 7) and the heterogeneous head model (Figure 10). Specifically, eight loops could reach a performance of only 45% for a voxel at the center of the brain at 7 T, while 32 loops achieved $\sim 70\%$ of the OPTXE. Compared with the case of the homogeneous sphere, performance maps were less uniform in the realistic head, especially at higher field strengths, reflecting the nonuniform geometry and tissue distribution which affects the propagation of the EM field.

4 | DISCUSSION

We introduced the OPTXE, a novel theoretical upper bound for the performance of transmit coils, and investigated its behavior using head-mimicking uniform spherical samples and a heterogeneous head model, for different magnetic field strengths and target excitations. The distribution of the OPTXE for single voxels across the diameter of the spherical sample resembled that reported for the UISNR.^{20,21} The resulting OPTXE presented rotational symmetry, had its minimum at the center and grew exponentially as the target voxel position approached the surface of the sphere. However, note that OPTXE cannot be equal to the UISNR, which by definition is scaled by the square of B_0 . Furthermore, the UISNR optimization constrains the receive sensitivity to be equal to one at the voxel of interest while minimizing noise everywhere in the sample, whereas the OPTXE optimization we proposed maximizes directly the ratio of transmit sensitivity and RF power deposition. As a result, the optimal RF shimming weights are not equal in the two cases, yielding different distributions of the net magnetic and electric field. The shape and amplitude of the ICP associated with OPTXE and UISNR for the same voxel are also different, except at the center of the object, where they are dominated by one mode.²⁴

The OPTXE decreased as B_0 increased for almost all of the cases considered in this work, except for the smallest spherical sample size, where the OPTXE slightly increased near the center when going from ultra-high to extreme fields (>10.5 T). This could be due to the RF wavelength

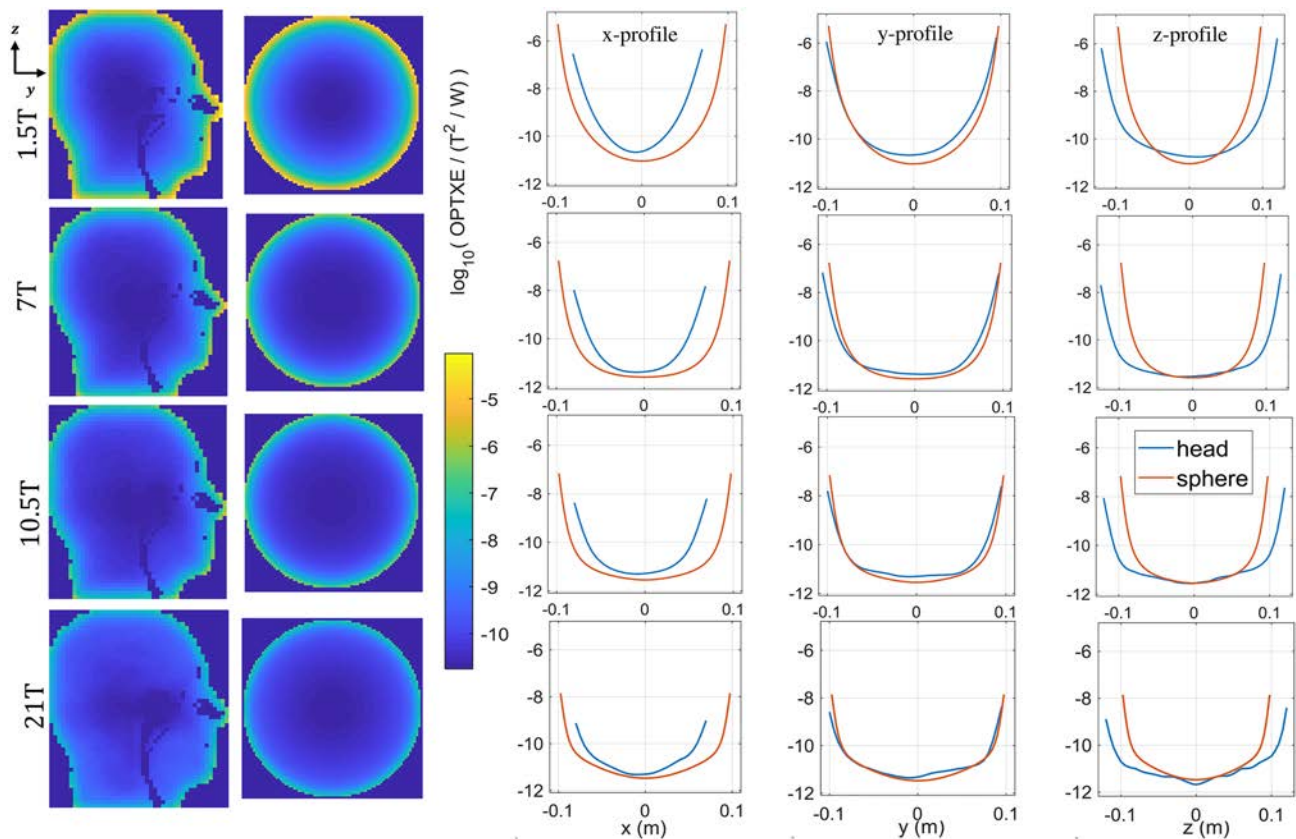


FIGURE 9 Comparison of the optimal transmit efficiency (OPTXE) in the heterogeneous head model and the head-mimicking uniform sphere as a function of voxel position and for different magnetic field strengths. OPTXE is plotted in logarithmic scale for the central sagittal plane of the “Duke” head model and the spherical sample with radius $a = 10$ cm, for $B_0 = 1.5, 7, 10.5$ and 21 T. OPTXE profiles along the x, y and z axes are in agreement between the two objects, especially for the case of the y-profile, for which the dimension of the head matches the radius of the sphere. OPTXE decreased with increasing field strength for both the heterogeneous head model and the uniform sphere

becoming small enough compared with the object to cause field-focusing effects near the center of the sphere.⁴⁴ Another difference with respect to previous work on UISNR is that in this study we calculated OPTXE not only for single voxels, but also for larger target excitation regions, which provides a more compact (single number vs. map) coil assessment, and more widely applicable benchmarks for optimal transmit coil design. We found the behavior of OPTXE to be similar for 2D and 3D excitation ROIs. In particular, OPTXE remained approximately constant for increasing size of the excitation region, until the radius of the ROI approached the radius of the spherical sample, at which point the high values observed for superficial voxels began to dominate the OPTXE within the ROI. However, while maximizing TXE, this scenario would result in a highly inhomogeneous B_1^+ distribution, with a nearly zero field in the central region. Using the same theoretical formalism, we showed that it could be possible to tradeoff a percentage of TXE and search for the eigenvector that minimizes B_1^+ inhomogeneity (Figure 5). We also observed that at UHF, especially for large objects, the OPTXE slightly decreased from its central value when the ROIs were sufficiently large to include intermediate voxels (Figure 4). This behavior suggests that it could be more challenging to optimize TXE over certain ROIs when their size is comparable with the wavelength, leading to field-focusing effects, or when both wavelength and field penetration are small compared with the size of the spherical sample.

The ICP yielding OPTXE at single voxels resembled the ICP associated with UISNR at the same locations.³¹ In particular, their shape was identical for the central voxel, consisting of distributed current loops precessing at the Larmor frequency around the direction of the main magnetic field (Video S1). This was expected, since only one mode survives at the center of the sphere,²⁴ and in both cases its role is to closely track spins precessing at the voxel of interest. The only difference is the opposite direction of the precession of the current loops, which accounts for the fact that for OPTXE it is the transmit sensitivity that is maximized, whereas for UISNR it is the receive sensitivity. These patterns could, for example, be achieved by quadrature birdcage coils.⁴⁵ At low fields, for voxels closer to the surface of the object, the ICP took the form of single loops alternating with figure-of-eight shapes, suggesting that surface quadrature coils⁴⁶ could be a better fit. At higher field strengths, the ICP for voxels away from the center became increasingly complex, suggesting that asymmetric quadrature coils might perform better than traditional closed loops. In fact, previous work showed that transmit/receive performance could be improved by considering the asymmetry of the EM field at high frequencies in the coil design process.^{47–49} Asymmetries and other effects due to wave propagation phenomena for increasing B_0 were even more

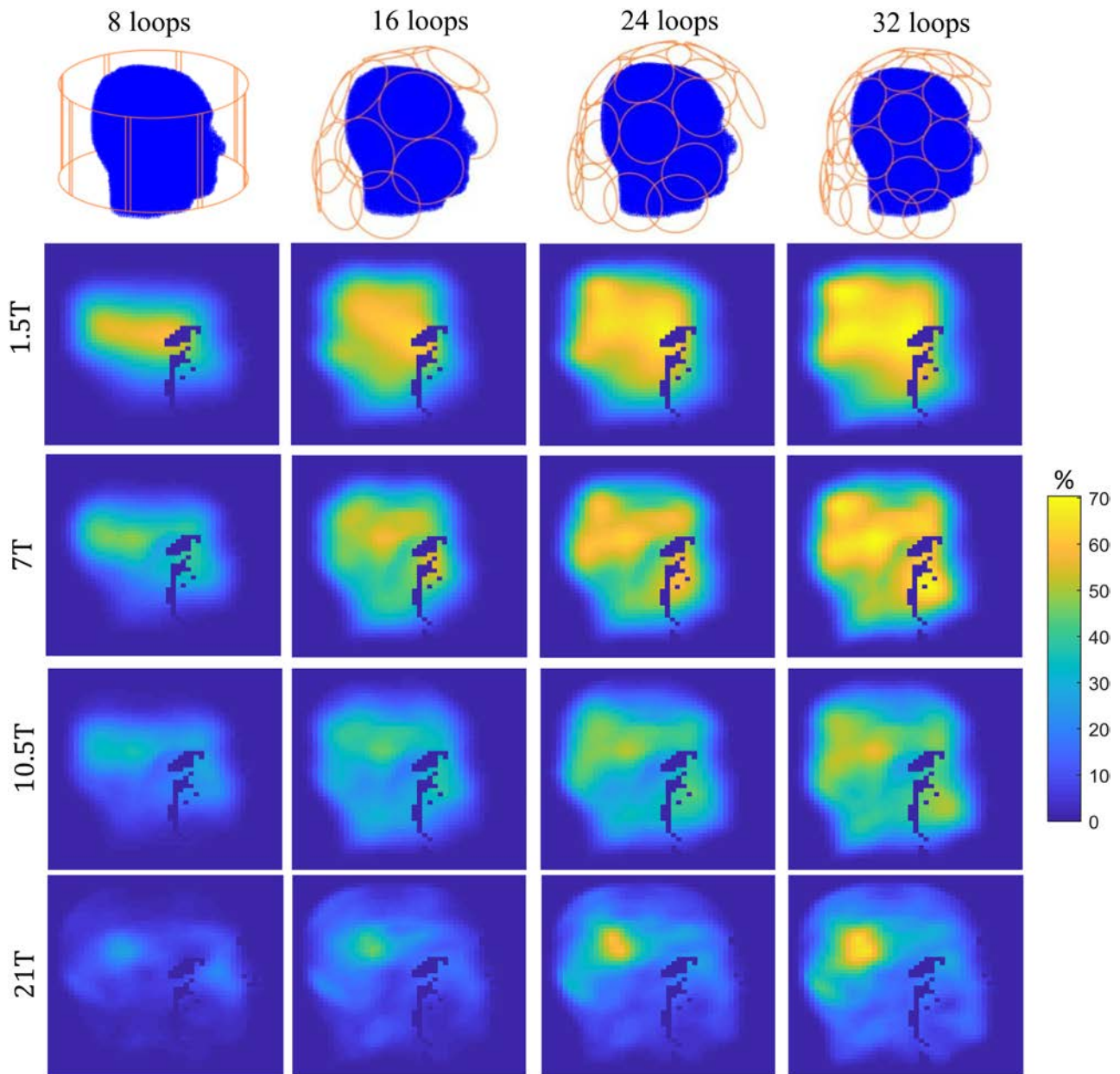


FIGURE 10 Absolute transmit performance of finite arrays with an increasing number of elements encircling the “Duke” realistic head model at different main magnetic field strengths. Performance maps displaying maximum TXE as a percentage of the OPTXE at each voxel of the central sagittal plane of “Duke” are shown for various finite arrays and for increasing B_0 . As for the case of the uniform sphere, absolute transmit performance becomes higher over a broader central region when the number of transmit loops increases

evident in the ICP for the case of 2D and 3D excitation ROIs (Videos S2 and S3). We also observed that the ICP became more localized and had considerably higher density around the excitation plane as the radius of the 2D ROI was increased. Interestingly, at 21 T, for the case of 3D ROIs, the ICP seemed concentrated around the two poles of the sphere. This behavior reflects our optimization approach, which normalizes with respect to total input power, regardless of how the power is distributed over the individual channels. As a result, while maximizing TXE, the highly localized ICP associated with large excitation ROIs do not represent realistic performance benchmarks for coil design. In fact, the power limits of individual channels in current MR transmit technology make it impractical to have large RF shims amplitudes concentrated on a small number of channels. Furthermore, despite optimal overall TXE, the B_1^+ distribution within the ROI would be highly inhomogeneous, with poor excitation in the central region that would compromise image quality. This issue could be avoided by trading off TXE for reduced B_1^+ inhomogeneity, as suggested above, and by excluding high order modes from the optimization. Figure S6 shows that by using such an approach it could be possible to also obtain more uniformly distributed current patterns, while still achieving a large percentage of the OPTXE. However, while the more distributed current patterns result in lower peak current density, the corresponding SAR increases overall (Figure S6). This is expected,¹ because in this

case the optimization was forced to prioritize B_1^+ homogeneity over TXE. This effect can also be seen in Figure 5, where SAR is clearly higher for the eigenvalues which reduce the CV of B_1^+ compared with those which maximize TXE.

Nevertheless, having realistic, distributed current patterns as a benchmark is useful, since we showed that it is possible to approach the optimal performance with finite arrays, especially when the coil configuration resembles the shape of the ICP. Array performance near the center (Figure 7) increased with the number of transmit coils surrounding the spherical sample at all field strengths. In fact, with more and smaller loops the overall array current patterns can better mimic the corresponding ICP, which form large distributed loops (Figure 3). Array performance was lower for voxels near the surface, where ICP consist of small localized loops that cannot be approximated using encircling arrays with a limited number of large loops. At low field, 16 transmit loops or more could achieve a higher performance over an extended excitation region, whereas such a region shrunk for higher B_0 . This suggests that to approach OPTXE at UHF, either more coils or different type of coils, for example, electric dipoles,²⁶ may be needed. While our results show general trends that provide physical insight into coil design, note that other factors, for example, losses associated with lumped elements, or imperfect matching and decoupling, could affect the TXE of actual transmit arrays.

Figure 8 also shows that the performance of an array depends strongly on how closely its elements can reproduce the corresponding ICP yielding OPTXE. More specifically, the belt-like arrays achieved considerably higher performance in those cases for which the ICP were localized around the excitation central plane and resembled a belt of loops (Figure 6). At 7 T, for example, the belt-like array with 32 loops could reach only 34% of the OPTXE for ROI radii smaller than $0.4a$, corresponding to distributed ICP, whereas for ROI radii between $0.6a$ and $0.9a$, with ICP focused along the central plane, the performance was as high as 93%. The radius of the 2D ROI associated with the largest performance increased with field strength. This can also be explained from the ICP in Figure 6, which show that focusing of the ICP around the excitation plane occurs for larger ROIs as the field strength increases.

The uniform dielectric sphere has been extensively used as a model of the human head to enable rapid analytic simulations to investigate ultimate performance limits and to explore dependencies on multiple design parameters. However, while useful for deriving general trends and guidelines for coil design, the spherical model is intrinsically limited when investigating the performance of specific head coil designs. In this work, we proposed a novel numerical framework to calculate the EM generated by basis functions defined on a shell enclosing the object, and employed it to calculate the OPTXE inside a realistic heterogeneous head model. Previously, researchers used random electric and magnetic dipoles distributed inside a thick voxelized layer surrounding the object as basis functions to calculate UISNR²¹ and the ultimate SAR amplification factor²² in realistic head models. Steensma et al reported using the same numerical approach to investigate the ultimate transmit performance in a realistic model of the human pelvis for a specific RF shimming excitation that imposes constructive interference at the central voxel.⁵⁰ Our implementation is intrinsically more accurate because it relies on SVD rather than randomized SVD to compress the numerical basis and it usually requires fewer degrees of freedom for discretizing the current sources. We validated our numerical approach against the analytical DGF computations for the case of a uniform sphere (Figure S7). We found that the relative error remained low ($\sim 2.5\%$) for an extended central region, but increased rapidly for voxels close to the surface, due to the staircase approximation of the curvature of the sphere. Such an error at the surface was expected when using voxelized geometries, but we showed that this could be considerably reduced by refining the resolution of the computational domain. While our numerical calculations for the realistic head were limited to a resolution of 5 mm, due to the computational time and memory capacity of the graphics processing unit, we expect higher accuracy than in Figure S7, because the surface curvature of the head model is smaller overall than for the sphere. Note also that obtaining accurate OPTXE values near the surface is not critical for assessing finite arrays, since their absolute performance is nearly 0% at these locations, where the OPTXE grows exponentially.

Previous work on UISNR using realistic head models²¹ demonstrated that the sphere with average brain electrical properties is a good approximation for the head, and the current work confirms such an observation for the case of the OPTXE (Figure 9). In particular, we showed that when the diameter of the sphere was equal to the dimension of the head, the sphere was expected to be a remarkably accurate approximation, even at the surface voxels (see the y-profile in Figure 9). This could be explained by the analytical and numerical (via SVD) eigenfunction expansions being similar for volumes with coinciding boundaries. In fact, as more modes are added while calculating the OPTXE, the resulting maximum eigenvalue distributions would become smoother and more similar for the two models, despite the higher inhomogeneity of the realistic head model. As a result, the calculation of the OPTXE in the realistic head model requires more modes for convergence, since EM fields with higher degrees of freedom, or higher spatial frequency, are required for generating the same smooth OPTXE distribution. The validity of the uniform sphere head approximation is also supported by the general trends of array performance with respect to field strength, and the number of coil elements remaining valid in the case of a realistic head model.

An advantage of the analytical framework is that the ICP for a spherical sample can be calculated in a straightforward manner as a weighted sum of the surface current basis modes, using the optimal RF shimming coefficients associated with OPTXE. Instead, in the case of a realistic head model, linear combinations of the discretized RWG basis functions do not necessarily result in continuous current patterns on the shell surrounding the object. Two promising approaches to calculate ICP for arbitrary dielectric objects and current-bearing surfaces have been recently proposed^{43,51} and these will be explored further in future work. Future work will also include exploring OPTXE and the associated ICP for body imaging at UHF MRI, where optimizing the TXE is critical.

In this work, we have introduced a formalism to calculate the OPTXE for RF shimming, but our approach could be generalized to parallel transmission. This would require adding the time dependence to Equation 2, in order for the phase and amplitude of the different transmit

channels to be updated at each time point. Note, however, that one advantage of using RF shimming is that, since the weights are fixed, there is a single optimal value and a single set of ICP associated with each excitation task, which facilitates the interpretation of the results. Furthermore, while the case of parallel transmission could be explored in simulation, it is not yet clear how a local power calibration could be noninvasively and robustly conducted in practice to evaluate the TXE of actual arrays with respect to the OPTXE. On the other hand, the global RF power covariance matrix for RF shimming can be measured experimentally.^{5–7} This could enable using absolute transmit performance—TXE/OPTXE—as a metric to evaluate actual RF coils in phantom experiments, similar to what was proposed for the receive case.²⁸ Furthermore, since the TXE (Equation 1) does not depend on acquisition parameters such as the SNR, no scaling factors would be needed for the comparison with the OPTXE. However, the proper hardware to measure the RF power correlation matrix and accurate B_1+ calculation would still be required.^{5–7,16}

5 | CONCLUSION

In this work, we introduced a formalism to calculate the OPTXE, which is an upper bound on transmit performance consistent with electrodynamic principles that is achievable for a given imaging sample and target excitation region. The OPTXE is independent of the particular array and coil combination, thus can be used as an absolute reference to evaluate both coil designs and RF shimming algorithms. We calculated OPTXE analytically for a uniform sphere with average brain electrical properties and proposed a novel numerical approach to calculate OPTXE for a realistic heterogeneous head model. We showed that the overall behavior of the OPTXE is similar for the two models. At UHF, finite arrays with as many as 32 transmit loops could approach OPTXE only in the central region of the object, suggesting that more transmit channels or different type of coils may be needed to optimize performance. We showed that ICP associated with OPTXE could provide useful insight into optimal coil design.

ACKNOWLEDGEMENTS

This work was supported in part by NIH R01 EB024536, NIH U01 EB025144, NSF 1453675, Skoltech-MIT Next Generation Program and it was performed under the rubric of the Center for Advanced Imaging Innovation and Research (CAI²R, www.cai2r.net), a NIBIB National Center for Biomedical Imaging and Bioengineering (NIH P41 EB017183).

ORCID

Ioannis P. Georgakis  <https://orcid.org/0000-0002-9672-928X>

Athanasios G. Polimeridis  <https://orcid.org/0000-0002-4552-3169>

Riccardo Lattanzi  <https://orcid.org/0000-0002-8240-5903>

REFERENCES

- Lattanzi R, Sodickson DK, Grant AK, Zhu Y. Electrodynamical constraints on homogeneity and radiofrequency power deposition in multiple coil excitations. *Magn Reson Med*. 2009;61:315–334.
- Deniz CM, Alon L, Brown R, Sodickson DK, Zhu Y. Specific absorption rate benefits of including measured electric field interactions in parallel excitation pulse design. *Magn Reson Med*. 2012;67:164–174.
- van den Bergen B, van den Berg CAT, Bartels LW, Lagendijk JJW. 7T body MRI: B1 shimming with simultaneous SAR reduction. *Phys Med Biol*. 2007;52:5429–5441.
- Eryaman Y, Tunc CA, Atalar E. Minimum SAR for RF shimming by allowing spatial phase variation. Proceedings of the 17th Annual Meeting of ISMRM, Honolulu, Hawaii, USA, 2009. p. 4777.
- Zhu Y. In vivo RF power and SAR calibration for multi-port RF transmission. Proceedings of the 17th Annual Meeting of ISMRM, Honolulu, Hawaii, USA, 2009. p. 2585.
- Alon L, Deniz CM, Lattanzi R, et al. An automated method for subject specific global SAR prediction in parallel transmission. Proceedings of the 18th Annual Meeting of ISMRM, Stockholm, Sweden, 2010. p. 780.
- Zhu Y, Alon L, Deniz CM, Brown R, Sodickson DK. System and SAR characterization in parallel RF transmission. *Magn Reson Med*. 2012;67:1367–1378.
- Vaughan JT, Adriany G, Snyder CJ, et al. Efficient high-frequency body coil for high-field MRI. *Magn Reson Med*. 2004;52:851–859.
- Vaughan JT, Hetherington HP, Otu JO, Pan JW, Pohost GM. High frequency volume coils for clinical NMR imaging and spectroscopy. *Magn Reson Med*. 1994;32:206–218.
- Hoult DI, Phil D. Sensitivity and power deposition in a high-field imaging experiment. *J Magn Reson Imaging*. 2000;12:46–67.
- Ibrahim TS, Lee R, Baertlein BA, Abduljalil AM, Zhu H, Robitaille PM. Effect of RF coil excitation on field inhomogeneity at ultra high fields: a field optimized TEM resonator. *Magn Reson Imaging*. 2001;19:1339–1347.
- Katscher U, Bornert P, Leussler C, van den Brink JS. Transmit SENSE. *Magn Reson Med*. 2003;49:144–150.
- Zhu Y. Parallel excitation with an array of transmit coils. *Magn Reson Med*. 2004;51:775–784.
- Padormo F, Beqiri A, Hajnal JV, Malik SJ. Parallel transmission for ultrahigh-field imaging. *NMR Biomed*. 2016;29(9):1145–1161.
- Zhu Y, Deniz CM, Alon L, Fautz HP, Sodickson DK. Understanding parallel transmit array efficiency. Proceedings of the 18th Annual Meeting of ISMRM, Stockholm, Sweden, 2010. p. 1518.

16. Deniz CM, Brown R, Lattanzi R, Alon L, Sodickson DK, Zhu Y. Maximum efficiency radiofrequency shimming: Theory and initial application for hip imaging at 7 Tesla. *Magn Reson Med*. 2013;69(5):1379-1388.
17. Ocali O, Atalar E. Ultimate intrinsic signal-to-noise ratio in MRI. *Magn Reson Med*. 1998;39:462-473.
18. Schnell W, Renz W, Vester M, Ermert H. Ultimate signal-to-noise ratio of surface and body antennas for magnetic resonance imaging. *IEEE Trans Antennas Propag*. 2000;48:418-428.
19. Ohliger MA, Grant AK, Sodickson DK. Ultimate intrinsic signal-to-noise ratio for parallel MRI: electromagnetic field considerations. *Magn Reson Med*. 2003;50:1018-1030.
20. Wiesinger F, Boesiger P, Pruessmann KP. Electrodynamics and ultimate SNR in parallel MR imaging. *Magn Reson Med*. 2004;52:376-390.
21. Guérin B, Villena JF, Polimeridis AG, et al. The ultimate signal-to-noise ratio in realistic body models. *Magn Reson Med*. 2017;78:1969-1980.
22. Guérin B, Villena JF, Polimeridis AG, et al. Computation of ultimate SAR amplification factors for radiofrequency hyperthermia in non-uniform body models: impact of frequency and tumour location. *Int J Hyperthermia*. 2018;34(1):87-100.
23. Pfrommer A, Henning A. The ultimate intrinsic signal-to-noise ratio of loop-and dipole-like current patterns in a realistic human head model. *Magn Reson Med*. 2018;80(5):2122-2138.
24. Lee HH, Sodickson DK, Lattanzi R. An analytic expression for the ultimate intrinsic SNR in a uniform sphere. *Magn Reson Med*. 2018;80(5):2256-2266.
25. Georgakis IP, Polimeridis AG, Lattanzi R. Ultimate intrinsic transmit efficiency for RF shimming. Proceedings of the 26th Annual Meeting of ISMRM, Paris, France, 2018. p. 139.
26. Lattanzi R, Wiggins GC, Zhang B, Duan Q, Brown R, Sodickson DK. Approaching ultimate intrinsic signal-to-noise ratio with loop and dipole antennas. *Magn Reson Med*. 2018;79(3):1789-1803.
27. Vaidya MV, Sodickson DK, Lattanzi R. Approaching ultimate intrinsic SNR in a uniform spherical sample with finite arrays of loop coils. *Concepts Magn Reson*. 2014;44:53-65.
28. Lattanzi R, Grant AK, Polimeni JR, et al. Performance evaluation of a 32-element head array with respect to the ultimate intrinsic SNR. *NMR Biomed*. 2009;23:142-151.
29. Celik H, Eryaman Y, Altıntaş A, Abdel-Hafez IA, Atalar E. Evaluation of internal MRI coils using ultimate intrinsic SNR. *Magn Reson Med*. 2004;52(3):640-649.
30. Gao Y, Chen W, Zhang X. Investigating the influence of spatial constraints on ultimate receive coil performance for monkey brain MRI at 7 T. *IEEE Trans Med Imaging*. 2018;37(7):1723-1732.
31. Lattanzi R, Sodickson DK. Ideal current patterns yielding optimal signal-to-noise ratio and specific absorption rate in magnetic resonance imaging: computational methods and physical insights. *Magn Reson Med*. 2012;68:286-304.
32. Chen G, Cloos M, Lattanzi R, Sodickson DK, Wiggins G. Bent Electric Dipoles: A Novel Coil Design Inspired by the Ideal Current Pattern for Central SNR at 7 Tesla. Proceedings of the 22nd Annual Meeting of ISMRM, Milan, Italy, 2014. p. 402.
33. Wiggins GC, Zhang B, Lattanzi R, Chen G, Sodickson DK. The electric dipole array: an attempt to match the ideal current pattern for central SNR at 7 Tesla. Proceedings of the 20th Annual Meeting of ISMRM, Melbourne, Australia, 2012. p. 541.
34. Haemer GG, Vaidya M, Collins CM, Sodickson DK, Wiggins GC, Lattanzi R. Approaching ultimate intrinsic specific absorption rate in radiofrequency shimming using high-permittivity materials at 7 Tesla. *Magn Reson Med*. 2018;80(1):391-399.
35. Prieto RE. A general solution to the maximization of the multidimensional generalized Rayleigh quotient used in linear discriminant analysis for signal classification. Acoustics, Speech and Signal Processing. *IEEE International Conference on Acoustics, Speech, and Signal Processing (ICASSP)*. 2003;VI: 157-160.
36. Ishimaru A. *Wave Propagation and Scattering in Random Media*. New York, NY: Academic Press; 1978.
37. Hochman A, Villena JF, Polimeridis AG, Silveira LM, White JK, Daniel L. Reduced-order models for electromagnetic scattering problems. *IEEE T Antenn Propag*. 2014;62(6):3150-3162.
38. Christ A, Kainz W, Hahn EG, et al. The virtual family—development of surface-based anatomical models of two adults and two children for dosimetric simulations. *Phys Med Biol*. 2009;55:N23-N38.
39. Tai CT. *Dyadic Green Functions in Electromagnetic Theory*. Institute of Electrical and Electronics Engineers. NJ: Piscataway; 1994.
40. Jackson JD. *Classical Electrodynamics*. New York: John Wiley & Sons; 1999.
41. Rao S, Wilton D, Glisson A. Electromagnetic scattering by surfaces of arbitrary shape. *IEEE Trans Antennas Propag*. 1982;30(3):409-418.
42. Georgakis IP, Giannakopoulos II, Litsarev MS, Polimeridis AG. A Fast Volume Integral Equation Solver with Linear Basis Functions for the Accurate Computation of Electromagnetic Fields in MRI. arXiv preprint arXiv:1902.02196. 2019.
43. Sodickson DK, Lattanzi R, Vaidya M, et al. The Optimality Principle for MR signal excitation and reception: New physical insights into ideal radio-frequency coil design. arXiv preprint arXiv:1808.02087. 2018.
44. Vaidya MV, Collins CM, Sodickson DK, Brown R, Wiggins GC, Lattanzi R. Dependence of B₁₊ and B₁₋ field patterns of surface coils on the electrical properties of the sample and the MR operating frequency. *Concepts Magn Reson Part B Magn Reson Eng*. 2016;46(1):25-40.
45. Hayes CE, Edelestein WA, Schenck JF, Mueller OM, Eash M. An efficient, highly homogeneous radiofrequency coil for whole-body NMR imaging at 1.5 T. *J Magn Reson*. 1985;63:622-628.
46. Kumar A, Bottomley PA. Optimized quadrature surface coil designs. *MAGMA*. 2008;21:41-52.
47. Reykowski A, Fischer H. V-cage and V-array: novel coil structures for higher field strengths. Proceedings of the 13th Annual Meeting of ISMRM, Miami Beach, FL, USA, 2005. p. 950.
48. Duan Q, Sodickson DK, Lattanzi R, Zhang B, Wiggins GC. Optimizing 7T spine array design through offsetting of transmit and receive elements and quadrature excitation. Proceedings of the 18th Annual Meeting of ISMRM, Stockholm, Sweden, 2010. p. 51.
49. Wiggins GC, Zhang B, Lattanzi R, Sodickson DK. B₁₊ and SNR optimization of high field RF coils through offsetting of transmit and receive elements. Proceedings of the 17th Annual Meeting of ISMRM, Honolulu, 2009. p. 2951.
50. Steensma BR, Van den Berg CAT, Klomp DWJ, Luijten PR, Raaijmakers AJE. Comparing realistic coil arrays to the ultimate intrinsic coil performance: a simulation study. ISMRM Workshop on Ultrahigh Field Magnetic Resonance, Dubrovnik, Croatia, 31 March–3 April, 2019.
51. Georgakis IP, Polimeridis AG, Lattanzi R. Ideal current patterns for optimal SNR in realistic heterogeneous head models. Proceedings of the 27th Annual Meeting of ISMRM, Montreal, Canada, 2019. p. 1036.
52. Martini E, Carli G, Maci S. An equivalence theorem based on the use of electric currents radiating in free space. *IEEE Antenn Wirel Propag Lett*. 2008;7: 421-424.

SUPPORTING INFORMATION

Additional supporting information may be found online in the Supporting Information section at the end of this article.

How to cite this article: Georgakis IP, Polimeridis AG, Lattanzi R. A formalism to investigate the optimal transmit efficiency in radiofrequency shimming. *NMR in Biomedicine*. 2020;33:e4383. <https://doi.org/10.1002/nbm.4383>

APPENDIX A.1: Mode expansion of the EM field inside a dielectric sphere

We constructed the DGF for a dielectric sphere using the method of superposition³⁹:

$$\bar{\mathbf{G}}(\mathbf{r}, \mathbf{r}') = \begin{cases} \bar{\mathbf{G}}_0(\mathbf{r}, \mathbf{r}') + \bar{\mathbf{G}}_s^{(1)}(\mathbf{r}, \mathbf{r}') & r \geq a \\ \bar{\mathbf{G}}_s^{(2)}(\mathbf{r}, \mathbf{r}') & r \leq a, \end{cases} \quad (\text{A.1})$$

where \mathbf{r}' is the position of the current sources, \mathbf{r} is the position at which the EM field is observed and a is the radius of the sphere. Since we are interested in calculating the EM field inside the sphere, we select the second branch:

$$\bar{\mathbf{G}}_s^{(2)}(\mathbf{r}, \mathbf{r}') = ik_0 \sum_{l=0}^{+\infty} \sum_{m=-l}^l [C_l \mathbf{M}_{l,m}(k_{in}, \mathbf{r}) \mathbf{M}_{l,m}^+(k_0, \mathbf{r}') + D_l \mathbf{N}_{l,m}(k_{in}, \mathbf{r}) \mathbf{N}_{l,m}^+(k_0, \mathbf{r}')]. \quad (\text{A.2})$$

k_0 and k_{in} are the wavenumbers in free space and inside the sphere, respectively, C_l and D_l are calculated by applying the Dirichlet boundary conditions,³¹ and the spherical vector wave functions are defined as:

$$\begin{aligned} \mathbf{M}_{l,m}(k, \mathbf{r}) &= \frac{1}{-i\sqrt{l(l+1)}} \nabla \times (\psi_{l,m} \mathbf{r}) \\ \mathbf{N}_{l,m}(k, \mathbf{r}) &= \frac{1}{k - i\sqrt{l(l+1)}} \nabla \times \nabla \times (\psi_{l,m} \mathbf{r}), \end{aligned} \quad (\text{A.3})$$

with k being the appropriate wave number at the position of interest. $\psi_{l,m} = j_l(kr)Y_{l,m}(\theta, \varphi)$ are the eigenfunctions that are solutions to the scalar wave equation with

$$Y_{l,m}(\theta, \varphi) = \sqrt{\frac{2l+1}{4\pi} \frac{(l-m)!}{(l+m)!}} P_l^m(\cos\theta) e^{im\varphi} \quad (\text{A.4})$$

where $P_l^m(\cos\theta)$ is the associated Legendre function of order (l, m) and j_l is the spherical Bessel function of order l . The superscript $+$ in Equation A.2 indicates that the spherical Hankel function of the first kind and order l is used in place of the spherical Bessel function of the same order.

The electric field inside the sphere can be calculated using Equations 7, 8, A.1 and A.2 as:

$$\begin{aligned} \mathbf{E}(\mathbf{r}) &= i\omega\mu_0 \int_{V'} \bar{\mathbf{G}}(\mathbf{r}, \mathbf{r}') \cdot \mathbf{J}(\mathbf{r}') dV' \\ &= i\omega\mu_0 \int_{S'} \bar{\mathbf{G}}_s^{(2)}(\mathbf{r}, \mathbf{r}') \cdot \mathbf{K}(\mathbf{r}') dS' \\ &= -\omega\mu_0 k_0 \int_{S'} \left\{ \sum_{l=0}^{+\infty} \sum_{m=-l}^l [C_l \mathbf{M}_{l,m}(k_{in}, \mathbf{r}) \mathbf{M}_{l,m}^+(k_0, \mathbf{r}') + D_l \mathbf{N}_{l,m}(k_{in}, \mathbf{r}) \mathbf{N}_{l,m}^+(k_0, \mathbf{r}')] \right\} \\ &\quad \cdot \left\{ \sum_{l'=0}^{+\infty} \sum_{m'=-l'}^{l'} -i\sqrt{l'(l'+1)} \left[W_{l',m'}^{(M)} \mathbf{X}_{l',m'}(\theta', \varphi') + W_{l',m'}^{(E)} \hat{\mathbf{r}} \times \mathbf{X}_{l',m'}(\theta', \varphi') \right] \right\} dS', \end{aligned} \quad (\text{A.5})$$

from which we can define the coefficients in Equation 9:

$$\begin{aligned} V_{(lm)}^M(l', m') &= C_l \int_{S'} \left[\mathbf{M}_{lm}^+(k_0, \mathbf{r}') \cdot \left(-i\sqrt{l'(l'+1)} \mathbf{X}_{l', m'}(\theta', \varphi') \right) \mathbf{W}_{l', m'}^{(M)} \right. \\ &\quad \left. + \mathbf{M}_{lm}^+(k_0, \mathbf{r}') \cdot \left(-i\sqrt{l'(l'+1)} \hat{\mathbf{r}} \times \mathbf{X}_{l', m'}(\theta', \varphi') \right) \mathbf{W}_{l', m'}^{(E)} \right] dS' \end{aligned} \quad (\text{A.6})$$

$$\begin{aligned} V_{(lm)}^N(l', m') &= D_l \int_{S'} \left[\mathbf{N}_{lm}^+(k_0, \mathbf{r}') \cdot \left(-i\sqrt{l'(l'+1)} \mathbf{X}_{l', m'}(\theta', \varphi') \right) \mathbf{W}_{l', m'}^{(M)} \right. \\ &\quad \left. + \mathbf{N}_{lm}^+(k_0, \mathbf{r}') \cdot \left(-i\sqrt{l'(l'+1)} \hat{\mathbf{r}} \times \mathbf{X}_{l', m'}(\theta', \varphi') \right) \mathbf{W}_{l', m'}^{(E)} \right] dS' \end{aligned}, \quad (\text{A.7})$$

where the vector spherical harmonics are defined as³⁹

$$\mathbf{X}_{lm}(\theta, \varphi) = \frac{1}{i\sqrt{l(l+1)}} (\hat{\mathbf{r}} \times \nabla) Y_{lm}(\theta, \varphi), \quad (\text{A.8})$$

in which $\hat{\mathbf{r}}$ is the unit vector in the radial direction. The integrals in Equations A.6 and A.7 can be solved by applying the orthogonality relations of the vector spherical harmonics,⁴⁰ yielding $\mathbf{v} = \mathbf{T}\mathbf{w}$ with $\mathbf{v} = [V_{lm}^M, V_{lm}^N]$, $\mathbf{w} = [\mathbf{W}_{lm}^{(M)}, \mathbf{W}_{lm}^{(E)}]$ and³¹:

$$\mathbf{T} = \begin{bmatrix} -i\sqrt{l(l+1)} h_l^{(1)}(k_0 b) C_l & 0 \\ 0 & \frac{-i\sqrt{l(l+1)} \partial}{k_0 b} \left[r h_l^{(1)}(k_0 r) \right]_{r=b} D_l \end{bmatrix}. \quad (\text{A.9})$$

We can then calculate the magnetic field in Equation 9 using Maxwell's equation, $\mathbf{B}(\mathbf{r}) = i/\omega \nabla \times \mathbf{E}(\mathbf{r})$, and the symmetrical relations of the vector wave functions.³⁹ Note that although we only consider electric current sources, the basis in Equation 8 can represent all possible EM field distributions within the sample because the currents equivalence principle can be formulated with either only electric or only magnetic currents.⁵² It should be noted that we used the $e^{i\omega t}$ harmonic time variation for all fields and currents, which is omitted for brevity.

APPENDIX A.2: Calculation of the transmit sensitivities and electric fields covariance matrices

For each mode, we can construct the transmit sensitivity matrix as:

$$\mathbf{B}_1^+(r_q) = \mathbf{B}_x + i\mathbf{B}_y = \sum_{l=0}^{l_{\max}} \sum_{m=-l}^l \mathbf{C}_{lm}(r_q) \mathbf{w}. \quad (\text{A.10})$$

$\mathbf{C}_{lm}(r_q)$ is a $Q \times 2$ matrix that includes both the divergence-free and curl-free contributions and accounts for the boundary conditions:

$$\mathbf{C}_{lm}(r_q) = -i\mu_0 k_0 k_{in} \left[\mathbf{N}_{lm}^x(k_{in}, r_q) + i\mathbf{N}_{lm}^y(k_{in}, r_q) \quad \mathbf{M}_{lm}^x(k_{in}, r_q) + i\mathbf{M}_{lm}^y(k_{in}, r_q) \right] \mathbf{T}. \quad (\text{A.11})$$

The RF power covariance matrix for the modes can be calculated as:

$$P_{\text{abs}} = \frac{1}{2} \int_V \sigma(\mathbf{r}) \mathbf{E}^*(\mathbf{r}) \cdot \mathbf{E}(\mathbf{r}) dV = \sum_{l=0}^{l_{\max}} \sum_{m=-l}^l \mathbf{w}^H \Phi_{lm} \mathbf{w}, \quad (\text{A.12})$$

where $\Phi_{l,m} = \mathbf{T}^H \mathbf{R}_L \mathbf{T}$ is a 2×2 diagonal matrix and \mathbf{R}_L is given by³¹:

$$\mathbf{R}_L = \frac{\sigma(\omega\mu_0 k_0)^2}{2} \begin{bmatrix} \int_0^a |j_l(k_{in}r)|^2 r^2 dr & 0 \\ 0 & \frac{1}{|k_{in}|^2} \int_0^a \left[\left| \frac{\partial [r j_l(k_{in}r)]}{\partial r} \right|^2 + l(l+1) |j_l(k_{in}r)|^2 \right] dr \end{bmatrix} \quad (\text{A.13})$$

and the global covariance matrix with dimensions $2N \times 2N$ for all the modes is:

$$\Phi_{\text{mode}} = \begin{bmatrix} \Phi_{0,0} & 0 & 0 \\ 0 & \ddots & 0 \\ 0 & 0 & \Phi_{l_{\max},l_{\max}} \end{bmatrix}. \quad (\text{A.14})$$